J Mater Sci

Electronic materials

Thermally stable epitaxial ZrN/carrier-compensated $Sc_{0.99}Mg_{0.01}N$ metal/semiconductor multilayers for thermionic energy conversion

Magnus Garbrecht[1,*], Ingrid McCarroll[1,2], Limei Yang[1], Vijay Bhatia[1], Bidesh Biswas[3,4,5], Dheemahi Rao[3,4,5], Julie M. Cairney[1,2], and Bivas Saha[3,4,5]

[1] *Australian Centre for Microscopy and Microanalysis, The University of Sydney, Camperdown, NSW 2006, Australia*
[2] *School of Aerospace, Mechanical and Mechatronic Engineering, The University of Sydney, Camperdown, NSW 2006, Australia*
[3] *Chemistry and Physics of Materials Unit, Jawaharlal Nehru Centre for Advanced Scientific Research, Bangalore 560064, India*
[4] *International Centre for Materials Science, Jawaharlal Nehru Centre for Advanced Scientific Research, Bangalore 560064, India*
[5] *School of Advanced Materials (SAMat), Jawaharlal Nehru Centre for Advanced Scientific Research, Bangalore 560064, India*

Received: 15 July 2019
Accepted: 14 October 2019

ABSTRACT

Epitaxial metal/semiconductor multilayers are attractive materials for a range of solid-state energy conversion devices. Applications include waste-heat-to-electrical energy conversion, hot-electron-based solar energy conversion in photocatalysis and photodiodes, optical hyperbolic metamaterials, and engineering thermal hyperconductivity. ZrN/ScN is among the first metal/semiconductor multilayer structures to also display promising thermal and electronic properties. However, for efficient thermionic transport, it is necessary to control and tune the Schottky barrier height at the metal/semiconductor interfaces, since this controls current flows across the superlattices' cross-plane directions. Sputter-deposited semiconducting ScN in ZrN/ScN multilayers contains a high concentration of *n*-type carriers, primarily due to oxygen impurities. This leads to a very small depletion width at metal/semiconductor interfaces, preventing thermionic transport. To overcome this challenge, the *n*-type carrier concentration of ScN has been reduced by Mg hole doping to $\sim 1.6 \times 10^{18}$ cm^{-3}. In this article, we report the growth of thermally stable epitaxial ZrN/carrier-compensated $Sc_{0.99}Mg_{0.01}N$ multilayers useful for thermionic emission-based devices. We present carrier concentration and transport regime calculations. Characterization of the microstructure and thermal stability was performed by combining aberration-corrected scanning transmission electron microscopy, energy-dispersive X-ray spectroscopy mapping, and atom probe tomography. The results show stoichiometric $Sc_{0.99}Mg_{0.01}N$ layers with a uniform magnesium concentration, and lattice-matched $ZrN/Sc_{0.99}Mg_{0.01}N$ growth with smooth and atomically sharp interfaces that are

Address correspondence to E-mail: magnus.garbrecht@sydney.edu.au

https://doi.org/10.1007/s10853-019-04127-x

Published online: 25 October 2019

thermally stable after 48 h at 950° C. The successful demonstration of thermally stable ZrN/carrier-compensated $Sc_{0.99}Mg_{0.01}N$ multilayers with a semiconductor carrier concentration of 2×10^{18} cm^{-3} is expected to enable efficient thermionic transport devices with improved properties.

Introduction

Ever since the 1960s, when *Esaki and Tsu* first proposed band structure engineering and resonant tunneling effects in materials with artificially structured periodic multilayers and superlattice heterostructures [1], semiconductor superlattices have made a profound impact [1–5]. Epitaxial lattice-matched GaAs/AlAs superlattices are used in several electronic, optoelectronic, and quantum electronic devices such as in quantum well lasers [6, 7], quantum cascade lasers [8, 9], and resonant tunneling diodes [10, 11]. In addition, semiconductor superlattices are widely used to study fundamental physics, materials science, and device engineering properties [12–14].

In contrast, the development of epitaxial metal/semiconductor multilayers and superlattices has been slow due to challenges with material compatibility and growth [15, 16]. Defect-free single-crystalline metal/semiconductor superlattices with atomically sharp interfaces and tunable Schottky barrier heights could lead to novel solutions in several branches of modern solid-state energy conversion. Examples include waste-heat-to-electrical energy conversion with thermionic transport of electrons [17–19], plasmon-induced hot-electron devices for photocatalysis [20, 21], photodiodes [22], photodetectors [23], optical hyperbolic metamaterials for engineering densities of photonic states [24, 25], tailored light absorption [26], emission and the demonstration of photonic hyperthermal conductivity [27–29]. Yet, from the initial demonstration of polycrystalline–metal/amorphous–dielectric heterojunctions such as $Al/Al_2O_3/Pb$ and Al/MgO/Pb in the 1960s [29–32], and the subsequent development of crystalline $Si/CoSi_2/Si$, AlAs/NiAl/AlAs, and GaAs/ErAs/GaAs heterojunctions [33–36], a lack of suitable metal and semiconductors with compatible crystal structures, lattice constants, and low surface and interface energies has hindered the development of epitaxial lattice-matched metal/semiconductor multilayer and superlattice growth until very recently [37, 38].

Epitaxial lattice-matched ZrN/ScN metal/semiconductor multilayers are one of the first demonstrations of such artificially structured metamaterials and have attracted significant interest in recent years due to their potential thermionic energy conversion applications [39]. Sputter-deposited ZrN/ScN multilayers exhibit atomically sharp interfaces and cube-on-cube epitaxial crystal growth on MgO substrates. However, due to the presence of an ~ 7% lattice mismatch between the MgO substrate and the nitride multilayers, threading dislocations occur that originate at the interface between the film and substrate, and thread through the film to the surface [40]. Thermal annealing performed inside inert ambient environments has demonstrated that these multilayers are stable at elevated temperatures (~ 950 °C), despite pipe diffusion of metallic atoms occurs along the threading dislocation lines [41]. Time-domain thermoreflectance (TDTR) measurements have shown that the thermal conductivity of these multilayers exhibits a minimum at a multilayer period thickness of ~ 4 nm at room temperature [42]. A minimum room-temperature thermal conductivity of 5 W/mK was realized in ZrN/ScN multilayers. By incorporating of heavy tungsten (W) in the ZrN and providing an additional alloy to scatter phonons, the thermal conductivity of (Zr,W)N/ScN multilayers was reduced to ~ 2 W/mK. This is highly desirable as low thermal conductivity is necessary for thermoelectric applications. Though the structural and thermal properties of these multilayers show promise for energy conversion applications, cross-plane electrical measurements and demonstration of reproducible thermionic energy transport in these multilayers have been proven challenging [39], limiting the applications so far.

Since the Schottky barrier height at metal/semiconductor interfaces determines current flow along the cross-plane or growth directions of the superlattices, it is necessary to determine and tune this height to achieve the desired electronic properties. However, the depletion width of the semiconductor at the metal/semiconductor interface also plays an

important role in the underlying current transport mechanism. For semiconductors with large carrier concentrations, carrier transport usually occurs by tunneling or field emission through a narrow depletion width (~ 2–3 nm) that eventually leads to Ohmic contact between metal and semiconductors, as shown schematically in Fig. 1a. The thermionic transport regime occurs when the carrier concentration of the semiconductor is sufficiently low, the depletion width becomes large (> tens of nm), and electrons are forced to transport above the Schottky barrier heights. For intermediate carrier concentrations and depletion widths, electron transport is determined by thermionic field emission, whereby thermally excited carriers tunnel through the barriers.

ScN is a promising indirect bandgap semiconductor, having recently attracted significant attention for its potential thermoelectric energy conversion [44–46], as an interlayer substrate material for GaN growth with low defect densities [47], and for the development of epitaxial defect-free metal/semiconductor superlattice metamaterials. The latter is due to the compatibility of the rocksalt crystal structure and transition metal nitrides exhibiting metallic properties (such as ZrN and HfN) [40]. Both pristine ScN and $Al_xSc_{1-x}N$ solid solution alloy films have demonstrated large piezoelectric coefficients that are useful for designing bulk and surface acoustic devices [48, 49]. For the application of ScN in metal/semiconductor superlattice devices, the effects of carrier concentration on the type of transport mechanism is therefore determined with a phenomenological theory [50] that compares the thermal energy k_B T with E_{00} (see Eq. 1) and is presented in Fig. 1b.

$$E_{00} = \frac{q\hbar}{2}\sqrt{\frac{N}{m^*\epsilon_s}} \tag{1}$$

where $m^* = 0.39\ m_0$ and $\epsilon_s = 12.3$ are the effective mass and dielectric permittivity of ScN, respectively, and N is its carrier concentration. When E_{00} is greater than ~ 5 k_B T, corresponding to a ScN carrier concentration of 2×10^{20} cm^{-3}, field emission or tunneling is expected to dominate the current transport at metal/semiconductor interfaces and lead to Ohmic contacts. On the other hand, when E_{00} is less than ~ 0.5 k_B T, corresponding to a ScN carrier concentration of 2×10^{18} cm^{-3} or less, thermionic emission is expected to dominate. For intermediate ScN carrier concentrations, thermionic field emission is expected to contribute to current transport. Therefore, for the achievement of thermionic emission and associated device properties, the carrier concentration of ScN needs to be reduced to less than 2×10^{18} cm^{-3}.

However, sputter-deposited ScN thin films exhibit a high n-type carrier concentration of (2–6) $\times 10^{20}$ cm^{-3} due to the presence of oxygen as impurity and possible nitrogen vacancies [51]. To

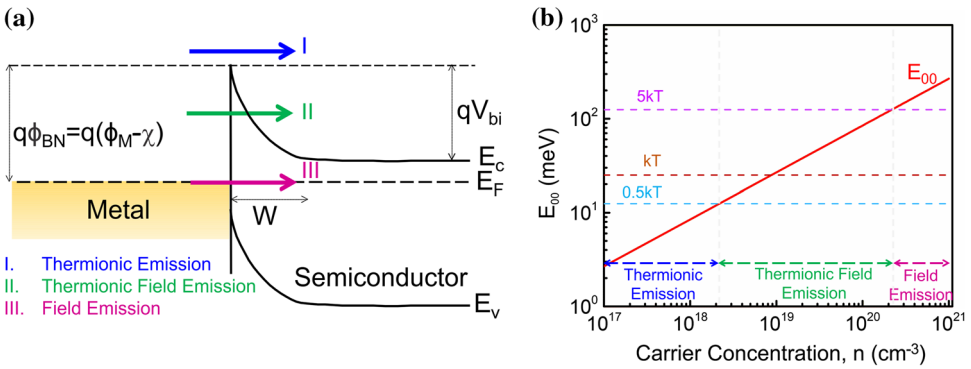

Figure 1 **a** Schematic representation of transport regimes at a metal/semiconductor interface. For high carrier concentrations in the semiconductor, field emission or tunneling dominate electron transport, while thermionic emission dominates transport at low carrier densities. Intermediate carrier concentration leads to thermionic field emission. Here, E_F is Fermi energy, E_C and E_V are conduction and valence bands, respectively, q is charge, V_{bi} is built-in potential, ϕ_{BN} is barrier height, ϕ_M is work function of the metal, and χ is the electron affinity of the semiconductor. **b** The three transport regimes at a metal/semiconductor interface calculated with Eq. 1 as a function of ScN carrier concentrations. For the energy E_{00} greater than 5 k_BT, tunneling is expected to dominate electrical transport, while for E_{00} lower than 0.5 k_BT, thermionic emission is expected to dominate. The figure shows that for achieving thermionic emission in ScN-based devices, the carrier concentration needs to be reduced below 2×10^{18} cm^{-3}.

overcome this important challenge and to reduce the carrier concentration of ScN, Mg is introduced inside ScN films, which acts as a hole-dopant. Previous results [52, 53] have shown that with an increase in Mg concentration, $Sc_{1-x}Mg_xN$ thin films exhibit a decrease in electron concentrations due to carrier compensation effects and exhibit a minimum electron concentration of 1.6×10^{18} cm^{-3} before being converted to a p-type semiconductor [52]. Recent photoemission and modeling analysis have also demonstrated that neither the oxygen impurity (O_N) nor the Mg hole doping (Mg_{Sc}) introduces any defect states inside ScN's bandgap, and the rigid band electronic structure remains unchanged [53]. Therefore, ZrN/compensated-and-low-carrier-concentration $Sc_{1-x}Mg_xN$ multilayers are expected to lead to larger depletion width and the possibility to demonstrate reproducible thermionic transport and device applications.

With that motivation, we demonstrate the growth of ZrN/carrier-compensated $Sc_{1-x}Mg_xN$ multilayers on MgO substrates and characterize their thermal stability and atomic scale structure. Specifically, we characterize the Mg dopant distribution with the aid of HRTEM and APT. A Mg concentration of 1% was utilized inside ScN that results in a reduced carrier concentration of $\sim 2 \times 10^{18}$ cm^{-3} inside the $Sc_{0.99}Mg_{0.01}N$ layers, which is measured with a separate individual $Sc_{0.99}Mg_{0.01}N$ thin film deposition and subsequent Hall measurement. To ensure that the current transport mechanism in multilayers is governed by the thermionic emission process, the $Sc_{0.99}Mg_{0.01}N$ semiconducting layer thickness of 7 nm was used.

Experimental

Film growth and treatment

$ZrN/Sc_{0.99}Mg_{0.01}N$ thin films were deposited on [001] MgO substrates by reactive DC-magnetron sputtering inside a load-locked turbo-molecular pumped high-vacuum deposition system with a base pressure of $\sim 4 \times 10^{-8}$ Torr (PVD Products, Inc.). The growth chamber can fit four targets and is equipped with three DC power supplies. The Sc (99.998% purity on metal basis), Zr (99.99%), and Mg (99.99%) targets had dimensions of 2 in. diameter and 0.25 in. thickness. All depositions were performed with an Ar/N_2 mixture of 6 sccm of N_2 and 4 sccm of Ar at a deposition pressure of 5 mTorr, and targets were sputtered in constant power mode. The substrates were maintained at 750 °C during deposition, as determined using an infrared pyrometer operated in the wavelength range of 0.8–1.1 μm, together with a thermocouple. The film structure was grown on (001) MgO by yielding nominal layer thickness values of 1 μm ZrN buffer/1 μm 7 nm/7 nm $ZrN/Sc_{0.99}Mg_{0.01}N$ multilayer/200 nm ZrN capping layer. The bottom 1 μm ZrN layer was deposited on MgO substrates for the current flow and cross-plane device measurements, as well as to serve as a buffer layer for the superlattices.

The superlattices were annealed (ramp rate = 20 °C min^{-1}) at 950 °C for either 24 h or 48 h in a 1.1 Pa (8.5 mTorr) forming gas ambient (5% H_2:95% N_2). The custom-designed annealing furnace consisted of a Boralectric tube heater inside a vacuum chamber that was evacuated to $< 9.3 \cdot 10^{-5}$ Pa ($7 \cdot 10^{-7}$ Torr) before continuously flowing 30 sccm forming gas to achieve a pressure of 8.5 mTorr. The 950 °C temperature of the inside heater wall and sample were verified with a dual-wavelength pyrometer.

Electron microscopy and atom probe tomography

The scanning/transmission electron microscopy (S/TEM) images and energy-dispersive X-ray spectroscopy maps were recorded by using an image- and probe-corrected and monochromated Themis-Z 60–300 kV equipped with a high-brightness XFEG source and Super-X EDS detector system for ultra-high count rates, operated at 300 kV. For STEM imaging and EDX mapping, the probe corrector was used to form a focused probe of 0.7 Å diameter. The Super-X EDX detector system enables the recording of high-spatial-resolution EDS maps. The EDS maps contain arrays of individual spectra as large as 4 k × 4 k pixel, and by color coding the elemental peak of the highest intensity for each spectrum/pixel is shown in the map. EDS maps with total counts well above 1,000,000 have been recorded for quantification. Absorption correction and applying the k-factor method yields a precision of about 2–3% atomic percent content in an area of known sample thickness at that count rates.

Atom probe tomography data were acquired on a laser-assisted CAMECA local electrode atom probe (LEAP) 4000X Si. Laser energy was set to 100 pJ with a pulse frequency of 200 kHz. The applied voltage changed dynamically in response to achieving a specified detection rate of 0.005 ions for every laser pulse. The analysis stage temperature was set to 60 K. Reconstruction of APT data was completed using IVAS 3.6.18. As a result of the changing evaporation field requirements for the ScN and ZrN layers, it was necessary to reconstruct the tip using the 'shank' reconstruction algorithm, and this algorithm assumes a constant shank angle along the length of the atom probe tip. The estimated shank angle used for reconstruction was 11°. Initial tip radius was calculated to be 24.71 nm, detector efficiency is 0.57, image compression factor was assumed to be 1.650, and a k-factor of 3.30 was used.

TEM lamellae and APT needles were prepared with a ThermoFisher Helios Xe Plasma FIB. Samples were coated with a 25-nm Au coating to prevent charging. A 500-nm Pt protective cap was deposited for both TEM and APT lift outs. TEM lamella were prepared using a 30 kV Xe at 60 nA followed by 15 nA for trenching and lift out. The TEM lift-out specimens were welded to Mo grids. Thinning was achieved with tilt angles of ± 2° and a beam current of 1 nA. Final thinning was at ± 2° and 300 pA, checking for electron transparency using a 2-kV electron beam with a SE detector. When the ROI was thin enough a 5 kV polish at 30 pA and ± 3° was used to remove beam-induced damage. TEM lamellae were prepared and thinned yielding both MgO [010] and [110] orientations. A wedge-shaped bar for atom probe samples was lifted out and welded to W posts on a grid. The atom probe needles were sharpened by annular milling with final cleaning at 10 kV and 50 pA.

Results and discussion

Film microstructure

A symmetric X-ray diffraction (XRD) spectrum from the multilayer structure reveals [002] oriented crystal growth with the main 002 peak located at 39.35° (see Fig. 2a), corresponding to a lattice constant of 4.57 Å. Previous XRD analysis had demonstrated that ZrN exhibits a lattice constant of 4.59 Å, while the lattice constant of Mg-doped ScN is very similar to that of pristine ScN (4.52 Å. Interference fringes arising from X-ray interference from different interfaces are clearly seen in the spectrum and a period thickness of ~ 12 nm is calculated from the fringe separations. The full width at half maxima (FWHM) of the rocking curve (ω-scan, see inset of Fig. 2a) corresponding to the main 002 2 θ- ω peak was 0.4°, indicating highly textured and nominally single-crystalline epitaxial growth.

Low-magnification TEM overview micrograph of the entire multilayer stack, (see Fig. 2b) shows that due to a 7% lattice mismatch between the ZrN buffer layer and MgO substrate threading dislocations are found mostly forming at the substrate/film interface, as described earlier in similar systems [40, 41]. An orientation relationship of ZrN [001] | | $Sc_{0.99}Mg_{0.01}N$ [001] was present throughout the film, demonstrated by the inset electron diffraction pattern (EDP). The individual layer thicknesses are consistent, and the layers themselves have a mostly flat morphology, apart from a slight curvature in the direct vicinity of the threading dislocations (Fig. 2c).

A few micrometers apart, but in non-regular intervals, extended defects (marked by an arrow in Fig. 2b) are found running vertically through the multilayer stack but not through the buffer layer. Figure 3a shows a HAADF-STEM micrograph of such a defect, with a characteristic kinking of the adjacent layers to both of its sides. Atomic resolution images (Fig. 3b) reveal those defects comprise voids: While an undisturbed lattice is maintained across the weak-contrast planes with a width of up to 5 nm, those regions are depleted of atoms with respect to the neighboring lattice. The elemental EDS maps in Fig. 3c, d confirm those regions to constitute voids, where a significant increase in oxygen signal along the defect line can be seen. Figure 3e shows the oxygen content histogram of a cross section through the defect as marked by the white rectangle in Fig. 3d.

Further, the voids do not originate at any sort of dislocation or similar defect at or nearby the substrate–film interface. On the contrary, they appear from the first $Sc_{0.99}Mg_{0.01}N$ layer on the ZrN buffer layer (Fig. 2b). A possible source of the voids could be shadowing during the growth, which has been previously found to introduce similar defects and voids in other nitride multilayers with similar individual layer thicknesses [54, 55]. The Schottky barrier

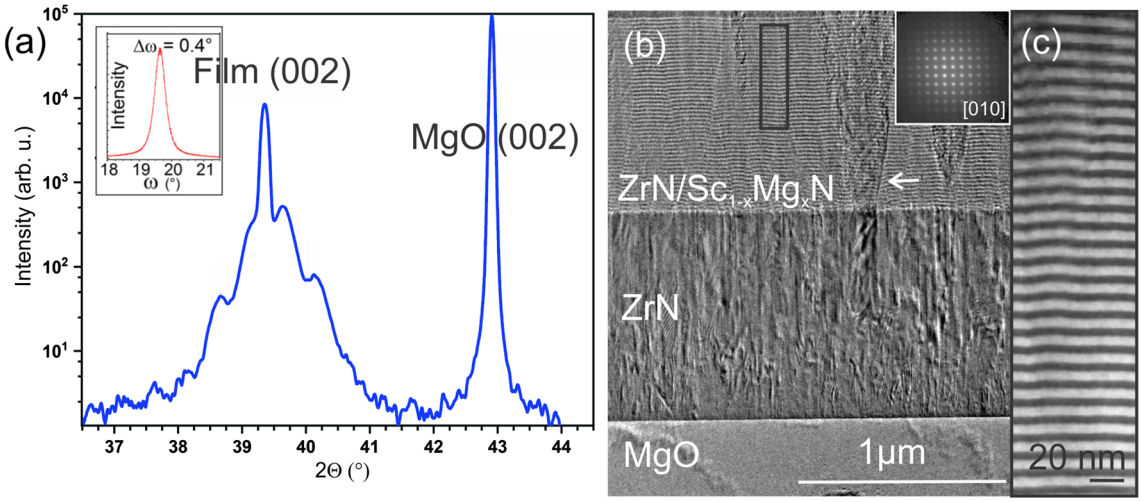

Figure 2 **a** XRD spectrum of the multilayer demonstrating 002 oriented epitaxial crystal growth. The FWHM of the rocking curve (ω-scan, in inset) of 0.4° indicates highly textured and nominally single-crystalline epitaxial growth. **b** Overview TEM micrograph of the entire multilayer stack comprising ZrN buffer- and capping layer and a 1-μm-think 7 nm/7 nm ZrN/$Sc_{1-x}Mg_xN$ multilayer. The inset EDP demonstrates the high-quality epitaxial growth. **c** Magnified micrograph of the region in the rectangle in (**b**) demonstrating mostly flat layers of even thickness and sharp interfaces.

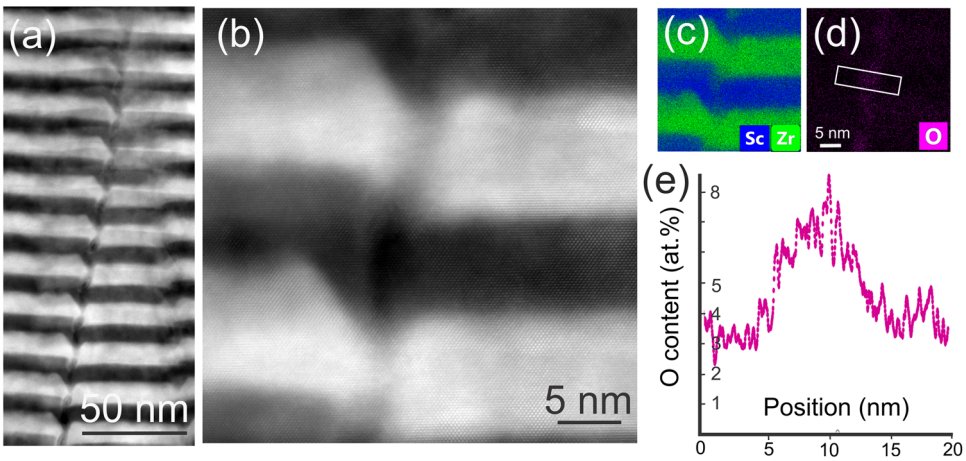

Figure 3 **a** Low- and **b** high-magnification STEM micrographs of the extended defect marked in Fig. 1 (**a**) by an arrow, showing that the defect comprises voids decorating the lattice planes in an 80° angle with respect to the growth surface. Elemental EDS maps **c**–**d** and a cross section **e** histogram plotting the oxygen content across the dark central region in (**b**) confirm this find.

height at the metal/semiconductor interfaces is not expected to change significantly due to the presence of such voids. However, the higher concentration of oxygen atoms (that acts an *n*-type dopants in ScN) inside the void regions could lead to internal shunts for current transport in the multilayers. However, as the concentration of such voids in this present study is rather small, their effects on the Schottky barrier height and on the current transport are expected to be rather small."

Dopant distribution

Stoichiometry within the superlattice, and in particular the Mg content within the ScN layers throughout the stack, is of importance, since $Sc_{1-x}Mg_xN$ with x = 0.01 was yielded during the growth process. Figure 4a shows an EDS map with more than 1 M counts in total (red: Mg, blue: Sc, green: Zr).

Following absorption correction for density and thickness, background modeling, and k-factor method for quantification, a total of 0.7 atomic % magnesium could be calculated but with a fitting

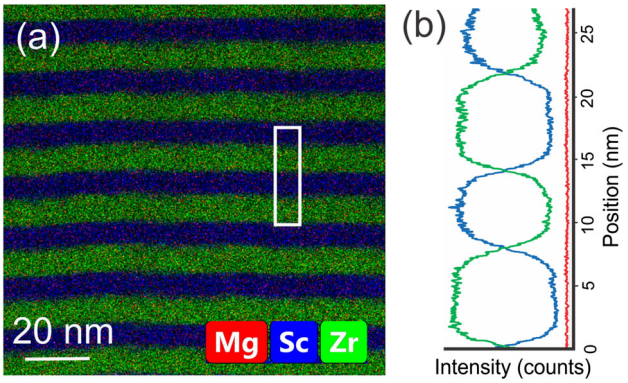

Figure 4 **a** STEM-EDS map showing the low Mg content within $Sc_{1-x}Mg_xN$ with nominally x = 0.01; however, the amount of Mg is at the edge of detectability with STEM-EDS even at such high-count rates, and too low for a concise quantification within the individual layers (**b**).

error amounting for ± 2.5 at. %, due to the difficulty of fitting very low contents of the weakly scattering Mg in the presence of the much heavier elements Sc and Zr. Consequently, when the stoichiometry profile Fig. 4b across the region marked by the white rectangle in (a) is plotted, the distribution of the Mg atoms cannot be unambiguously attributed to either the ZrN or ScN layers. Moreover, it cannot be ruled out that low levels of Mg might stem from the sample preparation during which Mg atoms might have been sputtered from the MgO substrate by the focused ion beam and re-deposited further up in the multilayer stack.

To provide further insight into the distribution of Mg within the ZrN and ScN layers, APT data were collected from a sharp needle-shaped sample (Fig. 5a, b). In an APT experiment, ions are extracted from the surface of the tip using high-field evaporation [56]. Field evaporation is not dependent on the mass of the elements, and thus all elements have the same probability of detection, relative to their abundance within the material, making it possible to identify the location of Mg atoms within 3D space. A 10-nm-thick section through the APT data indicates that Mg ions are distributed throughout the ScN layer, and that there may be a small amount of Mg distributed throughout the ZrN; see Fig. 5c. To clarify the distribution of Mg throughout these layers, a 1D concentration profile along the length of the 10-nm section (Fig. 5d) indicates that this quantity of Mg is below the APT background noise level (< 0.2 at. %), and it can therefore be interpreted from the data that there is no Mg within the ZrN layer. On initial inspection, the 1D concentration profile indicates that the interfaces between the two layers are not sharp. However, due to the variation in the electric fields required to evaporate the ScN versus the ZrN layer, delayed or early evaporation of the layer can occur. This preferential evaporation of the layers manifests itself as diffuse interfaces within the reconstructed data [57, 58], giving the impression of an inhomogeneous distribution of elements throughout the various layers. This particular artifact can cause preferential retention or evaporation of species, resulting in an apparent enrichment at the interface. We assume this to be the case in the current dataset, and therefore, we will provide comment only on the average composition of Mg within the ScN layer. To obtain an average composition of Mg within the layer, the interface region must be excluded from the calculations. An analysis of the average Mg concentration across each ScN layer is presented in Fig. 6. The average concentration across all interfaces is 0.73

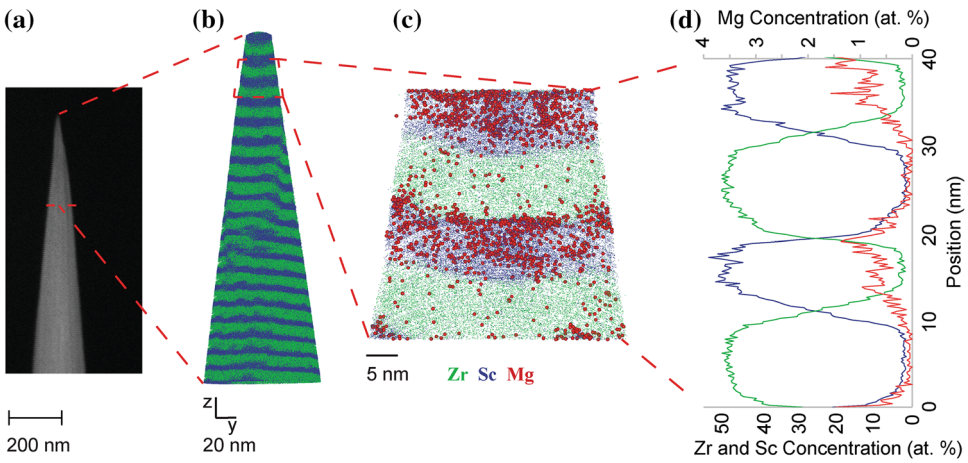

Figure 5 **a** Scanning EM image of FIB-prepared APT tip, **b** entire APT dataset. **c** An enlarged 10-nm-thick section of the tip shows the distribution of Mg throughout ZrN and ScN layers. **d** 1D concentration profile along the length direction corresponding to the section shown in (**c**).

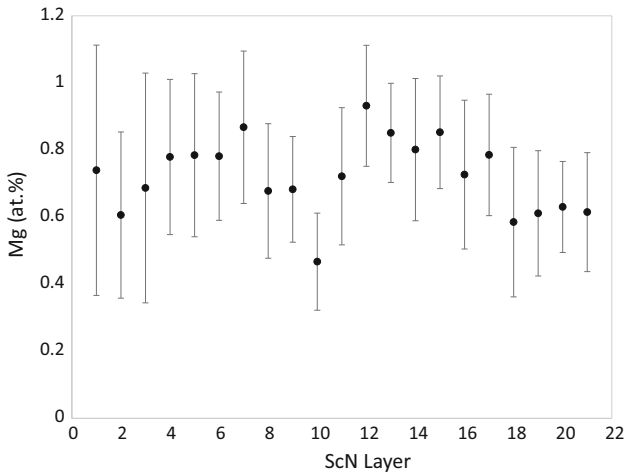

Figure 6 Average Mg concentration values in atomic percent calculated within each layer; the error bars represent one standard deviation.

at. % with a standard deviation of 0.24 at. %. The overall composition according to APT analysis is: 24.5 ± 2 at. % Sc, 24.6 ± 2 at. % Zr, 50.3 ± 1 at. % N, and 0.6 ± 0.1 at. % Mg. The errors in the overall composition are caused by overlapping peaks and thermal tails present in the mass spectrum.

Thermal stability

The effect of annealing on the microstructure was investigated as previous studies have shown that annealing to 950 °C for 24 h or longer of TiN-based metal/semiconductor superlattices leads to thermal instability by metal interdiffusion between the layers, which eventually leads to a loss of the multilayered structure [59]. In contrast, a different study on ZrN- and HfN-based metal/semiconductor superlattices showed that those systems were thermally stable (i.e., no detectable diffusion of metal atoms in between the layers except along threading dislocations) under the same annealing conditions of 950 °C for 24 h or longer [40].

To verify the thermal stability of the ZrN/$Sc_{1-x}Mg_xN$ systems, the deposited films were annealed for 48 h at 950 °C in forming gas ambient (see experimental details) using the same parameters as in [40] and [59]. Figure 7 shows EDS maps of the as-deposited (a) and 48 h annealed (b) samples. The metal and semiconductor layers are well separated both before and after heat the treatment, demonstrating thermal stability at high temperatures comparable to [40].

Conclusions

Epitaxial ZrN/compensated $Sc_{0.99}Mg_{0.01}N$ multilayers with a total thickness of ~ 1 µm were successfully deposited with high-vacuum magnetron sputtering and characterized by high-resolution XRD, STEM-EDS, and APT. Extended defects a few micrometers apart were found in the multilayer stacks that are comprised of oxygen-rich voids. STEM-EDS and APT analysis show stoichiometric $Sc_{0.99}Mg_{0.01}N$ layers with uniform magnesium concentrations and lattice-matched ZrN/$Sc_{0.99}Mg_{0.01}N$ growth with smooth, atomically sharp interfaces. The multilayers are thermally stable, with no obvious

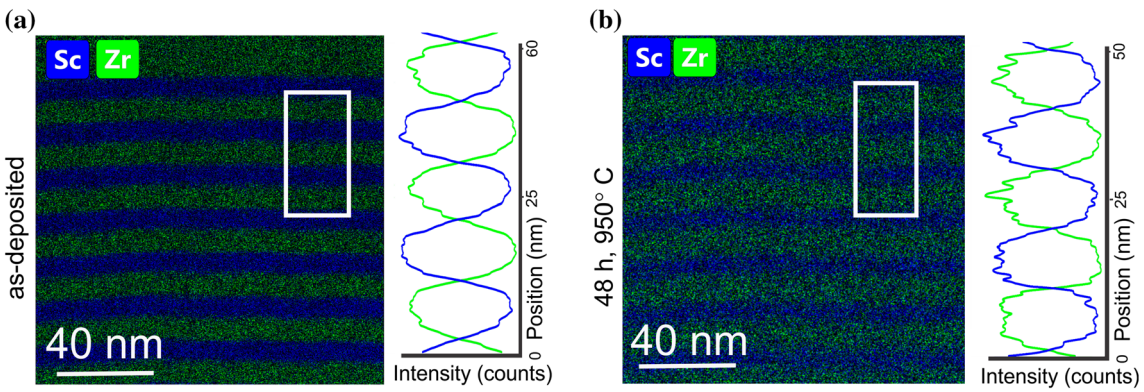

Figure 7 **a** EDX maps of ZrN/$Sc_{0.99}Mg_{0.01}N$ as deposited (**a**) and annealed at 950 °C in forming gas for 48 h (**b**), together with integrated line profiles shown from the regions in the white rectangles are presented. While the ZrN layers show a slight broadening after 48 h at 950 °C, the metal and semiconductor layers are still well separated after the heat treatment.

changes after 48 h at 950 °C. Due to the reduced carrier concentration of semiconducting layers from (2–6) × 10^{20} cm^{-3} in pristine ScN to 2 × 10^{18} cm^{-3} in $Sc_{0.99}Mg_{0.01}N$), the depletion width at metal/semiconductor interfaces is expected to increase from few nm to more than 10 s of nm, respectively, and leads to thermionic emission of electrons and reproducible electrical measurements. The successful demonstration of epitaxial ZrN/carrier-compensated $Sc_{0.99}Mg_{0.01}N$ multilayers is expected to result in tunable thermionic emission-based waste-heat recovery and hot-electron solar energy conversion devices.

Acknowledgements

The authors acknowledge the facilities of the Microscopy Australia node at the University of Sydney (Sydney Microscopy & Microanalysis). BB, DR, and BS acknowledge financial assistance from the International Centre for Materials Science (ICMS) and Sheikh Saqr Laboratory (SSL) of Jawaharlal Nehru Centre for Advanced Scientific Research (JNCASR). The authors acknowledge Mr. Abhijeet Chatterjee for assistance with HRXRD measurements.

Author contributions

All authors contributed to this paper and have approved the final version of the manuscript. M.G. planned this study and carried out all TEM experiments, data analysis and plotting, and prepared figures. I. McC. carried out all APT experiments, data analysis and plotting, and figure preparation. L.Y. and V.B. prepared TEM and APT samples and read and commented on the manuscript. J.M.C. oversaw APT experiments, contributed to data interpretation, and commented on the manuscript. B.B. and D.R. carried out XRD characterization and transport regime calculations. B.S. conceptualized the research, performed sample growth, and read and commented on the manuscript.

Compliance with ethical standards

Conflict of interest The authors declare no conflict of interest.

References

[1] Tsu R, Esaki L (1973) Tunneling in a finite superlattice. Appl Phys Lett 22:562–564

[2] Esaki L, Chang LL (1974) New transport phenomenon in a semiconductor "superlattice". Phys Rev Lett 33:495

[3] Esaki K (1988) A bird's-eye view on the evolution of semiconductor superlattices and quantum wells. Electronic structure of semiconductor heterojunctions. Springer, Dordrecht, pp 56–69

[4] Esaki L, Tsu R (1970) Superlattice and negative differential conductivity in semiconductors. IBM J Res Dev 14:61–65

[5] Sai-Halasz GA, Tsu R, Esaki L (1977) A new semiconductor superlattice. Appl Phys Lett 30:651–653

[6] Dassesasse JM, Holonyak N Jr, Sugg AR, Richard TA, El-Zein N (1990) Hydrolyzation oxidation of AlxGa1 − xAs-AlAs-GaAs quantum well heterostructures and superlattices. Appl Phys Lett 57:2844

[7] Nakamura S, Senoh M, Nagahama S, Iwasa N, Yamada T, Matsushita T, Kiyoku H, Sugimoto Y (1996) InGaN multi-quantum-well-structure laser diodes with cleaved mirror cavity facets. Jpn J Appl Phys 35:74

[8] Faist J, Capasso F, Sivco DL, Sirtori C, Hutchinson AL, Cho AY (1994) Quantum Cascade Laser. Science 264:553–556

[9] Faist J, Capasso F, Sivco DL, Hutchinson AL, Sirtori C, Chu SNG, Cho AY (1994) Quantum cascade laser: temperature dependence of the performance characteristics and high T_0 operation. Appl Phys Lett 65:2901–2903

[10] Kastrup J, Hey R, Ploog KH, Grahn HT, Bonilla LL, Kindelan M, Moscoso M, Wacker A, Galán J (1997) Electrically tunable GHz oscillations in doped GaAs–AlAs superlattices. Phys Rev B 55:2476

[11] Smith RP, Allen ST, Reddy M, Martin SC, Liu J, Muller RE, Rodwell MJW (1994) 0.1 μm Schottky-collector AlAs/GaAs resonant tunneling diodes. IEEE Electron Device Lett 15:295

[12] Dingle R, Stormer HL, Gossard AC, Wiegmann W (1978) Electron mobilities in modulation-doped semiconductor heterojunction superlattices. Appl Phys Lett 33:665

[13] Helm M, England P, Colas E, DeRosa F, Allen SJ Jr (1989) Intersubband emission from semiconductor superlattices excited by sequential resonant tunnelling. Phys Rev Lett 63:74

[14] Capasso F (1983) Band-gap engineering via graded gap, superlattice, and periodic doping structures: applications to novel photodetectors and other devices. J Vac Sci Technol, B 1:457

[15] Sands T, Palmstrom CJ, Harbison JP, Keramidas VG, Tabatabaie N, Cheeks TL, Ramesh R, Silberberg Y (1990) Stable and epitaxial metal/III-V semiconductor heterostructures. Mater Sci Rep 5:99–170

[16] Zhu J, Carter CB, Palmstrom CJ, Mounier S (1990) Microstructure of epitactically grown GaAs/ErAs/GaAs. Appl Phys Lett 56(14):1323
[17] Vashaee D, Shakouri A (2004) Improved thermoelectric power factor in metal-based superlattices. Phys Rev Lett 92:106103
[18] Mahan GD, Woods LM (1998) Multilayer thermionic refrigeration. Phys Rev Lett 80:4016
[19] Bian Z, Shakouri A (2006) Enhanced solid-state thermionic emission in nonplanar heterostructures. Appl Phys Lett 88:012102
[20] Sakhdari M, Hajizadegan M, Farhat M, Chen P (2016) Efficient, broadband and wide-angle hot-electron transduction using metal-semiconductor hyperbolic metamaterials. Nano Energy 26:371
[21] Garbrecht M, Hultman L, Fawey MH, Sands TD, Saha B (2018) Tailoring of surface plasmon resonances in TiN/$(Al_{0.72}Sc_{0.28})N$ multilayers by dielectric layer thickness variation. J Mater Sci 53(6):4001–4009. https://doi.org/10.1007/s10853-017-1837-4
[22] van Zeghbroeck BJ, Patrick W, Halbout JM, Vettiger P (1988) 105-GHz bandwidth metal-semiconductor-metal photodiode. IEEE Electron Device Lett 9(10):527–529
[23] Soole JBD, Schumacher H (1991) InGaAs metal-semiconductor-metal photodetectors for long wavelength optical communications. IEEE J Quantum Electron 27(3):737–752
[24] Saha B, Naik GV, Saber S, Akatay C, Stach EA, Shalaev VM, Boltasseva A, Sands TD (2014) Understanding the Rocksalt-to-Wurtzite phase transformation through microstructural analysis of (Al, Sc)N epitaxial thin films. Phys Rev B 90:125420
[25] Naik GV, Saha B, Liu J, Saber SM, Stach E, Irudayaraj JMK, Sands TD, Shalaev VM, Boltasseva A (2014) Epitaxial superlattices with titanium nitride as a plasmonic component for optical hyperbolic metamaterials. Proc Natl Acad Sci 111:7546
[26] Maccaferri N, Zhao Y, Isoniemi T, Iarossi M, Parracino A, Strangi G, De Angelis F (2019) Hyperbolic meta-antennas enable full control of scattering and absorption of light. Nano Lett 19(3):1851–1859
[27] Liu J, Narimanov E (2015) Thermal hyperconductivity: radiative energy transport in hyperbolic media. Phys Rev B 91:041403(R)
[28] Guo Y, Jacob Z (2013) Thermal hyperbolic metamaterials. Opt Express 21(12):15014
[29] Lambe J, Jaklevic RC (1968) Molecular vibration spectra by inelastic electron tunneling. Phys Rev 165:821
[30] Jaklevic RC, Lambe J (1966) Molecular vibration spectra by electron tunneling. Phys Rev Lett 17:1139
[31] Jaklevic RC, Lambe J (1975) Experimental study of quantum size effects in thin metal films by electron tunneling. Phys Rev B 12:4146
[32] Jaklevic RC, Lambe J, Mikkor M, Vassell WC (1971) Observation of electron standing waves in a crystalline box. Phys Rev Lett 26:88
[33] Rosencher E, Delage S, Campidelli Y, Arnaud D'Avitaya F (1984) Transistor effect in monolithic Si/$CoSi_2$/Si epitaxial structures. Electron Lett 20(19):762–7643
[34] Tabatabaie N, Sands T, Harbison JP, Gilchrist HL, Keramidas VG (1988) Negative differential resistance in AlAs/NiAl/AlAs heterostructures: evidence for size quantization in metals. Appl Phys Lett 53:2528–2530
[35] Stoffel NG, Palmstrom CJ, Wilkens BJ (1991) Ion channeling measurement of the lattice registry of ultrathin ErAs layers in GaAs/ErAs/GaAs (001) heterostructures. Nucl Instrum Methods Phys Res B 56(57):792
[36] Kadow C, Fleischer SB, Ibbetson JP, Bowers JE, Gossard AC, Dong JW, Palmstrom CJ (1999) Self-assembled ErAs islands in GaAs: growth and subpicosecond carrier dynamics. Appl Phys Lett 75:3548
[37] Saha B, Saber S, Naik GV, Boltasseva A, Stach E, Kvam EP, Sands TD (2015) Development of epitaxial $Al_xSc_{1-x}N$ for artificially structured metal/semiconductor superlattice metamaterials. Phys Stat Sol B 252:251
[38] Saha B, Shakouri A, Sands TD (2018) Rocksalt nitride metal/semiconductor superlattices: a new class of artificially structured materials. Appl Phys Rev 5:021101
[39] Zebarjadi M, Bian Z, Singh R, Shakouri A, Wortman R, Rawat V, Sands TD (2009) Thermoelectric transport in a ZrN/ScN superlattice. J Electron Mater 38(7):960–963
[40] Garbrecht M, Schroeder JL, Hultman L, Birch J, Saha B, Sands TD (2016) Microstructural evolution and thermal stability of HfN/ScN, ZrN/ScN, and $Hf_{0.5}Zr_{0.5}N$/ScN metal/semiconductor superlattices. J Mater Sci 51:8250. https://doi.org/10.1007/s10853-016-0102-6
[41] Garbrecht M, Saha B, Schroeder JL, Hultman L, Sands TD (2017) Dislocation-pipe diffusion in nitride superlattices observed in direct atomic resolution. Sci Rep 7:46092
[42] Rawat V, Koh YK, Cahill DG, Sands TD (2009) Thermal conductivity of (Zr, W)N/ScN metal/semiconductor multilayers and superlattices. J Appl Phys 105:024909
[43] Gall D, Petrov I, Hellgren N, Hultman L, Sundgren JE, Green JE (1998) Growth of poly- and single-crystal ScN on MgO(001): role of low-energy N_2^+ irradiation in determining texture, microstructure evolution, and mechanical properties. J Appl Phys 84:6034
[44] Kerdsongpanya S, van Nong N, Pryds N, Zukauskaite A, Jensen J, Birch J, Lu J, Hultman L, Wingqvist G, Eklund P

(2011) Anomalously high thermoelectric power factor in epitaxial ScN thin films. Appl Phys Lett 99:232113

[45] Kerdsongpanya S, Alling B, Eklund P (2012) Effect of point defects on the electronic density of states of ScN studied by first-principles calculations and implications for thermoelectric properties. Phys Rev B 86:195140

[46] Burmistrova PV, Maassen J, Favaloro T, Saha B, Salamat S, Rui Koh Y, Lundstrom MS, Shakouri A, Sands TD (2013) Thermoelectric properties of epitaxial ScN films deposited by reactive magnetron sputtering onto MgO(001) substrates. J Appl Phys 113:153704

[47] Moram MA, Zhang Y, Kappers MJ, Barber ZH, Humphreys CJ (2007) Dislocation reduction in gallium nitride films using scandium nitride interlayers. Appl Phys Lett 91:152101

[48] Akiyama M, Kamohara T, Kano K, Teshigahara A, Takeuchi Y, Kawahara N (2009) Enhancement of piezoelectric response in scandium aluminum nitride alloy thin films prepared by dual reactive cosputtering. Adv Mater 21:593

[49] Fichtner S, Wolff N, Lofink F, Kienle L, Wagner B (2019) AlScN: a III-V semiconductor based ferroelectric. J Appl Phys 125:114103

[50] Sze SM (1981) Physics of semiconductor devices, 2nd edn. Wiley, New York

[51] Biswas B, Saha B (2019) Development of semiconducting ScN. Phys Rev Mater 3:020301

[52] Saha B, Garbrecht M, Perez-Taborda JA, Fawey MH, Koh YR, Shakouri A, Martin-Gonzalez M, Hultman L, Sands TD (2017) Compensation of native donor doping in ScN: carrier concentration control and p-type ScN. Appl Phys Lett 110:252104

[53] Nayak S, Baral M, Gupta M, Singh J, Garbrecht M, Ganguli T, Shivaprasad SM, Saha B (2019) Rigid-band electronic structure of scandium nitride across the n-type to p-type carrier transition regime. Phys Rev B 99:161117(R)

[54] Hultman L, Wallenberg LR, Shinn M, Barnett SA (1992) Interdiffusion studies of single crystal TiN/NbN superlattice thin films. J Vac Sci Technol, A 10:1618

[55] Garbrecht M, Hultman L, Fawey MH, Sands TD, Saha B (2017) Void-mediated coherency-strain relaxation and impediment of cubic-to-hexagonal transformation in epitaxial metastable metal/semiconductor TiN/$Al_{0.72}Sc_{0.28}N$ multilayers. Phys Rev Mater 01:033402

[56] Gault B, Moody MP, Cairney JM, Ringer SP (2012) Atom probe microscopy. Springer, New York

[57] Mazumder B, Purohit V, Gruber M, Vella A, Vurpillot F, Deconihout B (2015) Challenges in the study of Fe/MgO/Fe interfaces using 3D atom probe. Thin Solid Films 589:38–46

[58] Marquis EA, Geiser BP, Prosa TJ, Larson DJ (2011) Evolution of tip shape during field evaporation of complex multilayer structures. J Microsc 241:225–233

[59] Schroeder JL, Saha B, Garbrecht M, Schell N, Sands TD, Birch J (2015) Thermal stability of epitaxial cubic-TiN/(Al, Sc)N metal/semiconductor superlattices. J Mater Sci 50:3200–3206. https://doi.org/10.1007/s10853-015-8884-5